DESTRESS

Demonstration of soft stimulation treatments
of geothermal reservoirs

Deliverable WP 3.2: Workflows for seismic risk assessment for soft stimulations

WP 3.2: Workflows for seismic risk assessment for soft stimulations based on high quality datasets

Authors: F. Grigoli[1], M. Broccardo[1], A. Mignan[1], B. Paap[2], A. Verdel[2] and S. Wiemer[1]

[1] ETH-Zurich, Swiss Seismological Service (SED), Zurich, Switzerland

[2] TNO, Applied Geosciences, Utrecht, Netherlands

Lead Beneficiary	
Type	☒ R - report, document etc. ☐ OTHER - software, technical diagram etc. ☐ DEM - demonstrator, pilot etc. ☐ E - ethics ☐ DEC - website, patent filing etc.
Status	☐ Draft ☒ WP manager accepted ☒ Project coordinator accepted
Dissemination level	☒ PU - Public ☐ CO - Confidential: only for members of the consortium
Contributors	☐ 1-GFZ ☐ 5-GES ☐ 9-GTL ☐ 13-SNU ☐ 2-EnB ☒ 6-TNO ☐ 10-UoS ☐ 14-KIC ☐ 3-ESG ☒ 7-ETH ☐ 11-TUD ☐ 15-ECW ☐ 4-UoG ☐ 8-GTN ☐ 12-NEX ☐ 16-WES
Creation date	23.01.2019
Last change	27.02.2019
Version	Final
Due date	28.02.2019
Submission date	12.03.2019

This project has received funding from the European Union's
Horizon 2020 research and innovation programme
under grant agreement No 691728

List of content

List of Figures

List of Table

I. Introduction: The ATLS

This public report entitled "***Workflows for seismic risk assessment for soft stimulations***" corresponds to the Deliverable 3.2 of the ***European Destress*** project. This comprehensive report is done on the framework of the WP3 dealing with "Risk management workflows for deep geothermal energy" and involved the scientific staff from ETH (Switzerland) and TNO (The Netherlands).

In recent years, seismicity induced by industrial operations has become an important topic of public interest. In many cases, earthquakes occurring in the vicinity of industrial facilities carrying underground operations were felt by the population, caused damages to private buildings, and increased the public concern about the development of these industrial activities (Ellsworth 2013). The increasing number of reported cases of such " man-made " earthquakes and their strong socio-economic impact has raised intense public debates and the interest of the non-scientific community on this topic (Grigoli et al. 2017). Such activities include water impoundment, mining, fluid subsurface resulting from operations related to hydrocarbon extraction, hydraulic fracturing for shale gas exploitation, wastewater injection, hydrocarbon storage operations, CO2 geological sequestration and hydraulic stimulation of geothermal fields. The stress perturbations produced by underground industrial activities, when proximal to seismogenic structures, might generate earthquakes. Fluid injection and consequent pore pressure alteration may also create new fractures and/or alter the frictional condition on existing faults, triggering new failures. The term " induced seismicity " generally refers to anthropogenic seismic events in a wide sense, however several studies (e.g. McGarr and Simpson 1997, Shapiro et al. 2010, Dahm et al. 2013) tend to make a clear distinction between "pure" induced and triggered seismicity. In the first case, induced seismic events are entirely controlled by stress changes caused by human operations and the whole rupture process, including its size, is driven by this stress (Dahm et al. 2013). In triggered seismicity the tectonic stress plays a primary role, while the human activity contributes only for a small fraction of the stress change. However, when close to tectonic faults, such (even small) stress changes can cause a loaded fault to fail. In this case, human operations are the trigger for an earthquake that would have occurred naturally in any case, but likely at a later time (Dahm et al. 2013). Furthermore, since these operations act only to accelerate the process of tectonic stress release, the magnitudes of such earthquakes can be large, depending on the amount of elastic strain energy accumulated on the fault due to tectonic loading and the fault dimensions. In this sense, a large earthquake could be triggered by minor induced stress changes, if the fault is prone to rupture. In this report we will use the term induced seismicity with is general meaning, as synonym of the anthropogenic seismicity.

The problem of induced seismicity is particularly important for the future development of deep geothermal energy in Europe which, despite his huge potential, it is still a small fraction of the total energy produced from renewable sources. One of the main obstacles to this development is that the high fluid pressures and the large fluid volumes injected during hydraulic stimulation operations may, induce or trigger seismic events that can be felt by the population, reducing the public acceptance of deep geothermal energy exploitation projects. Induced seismicity is thus an unwanted product of such industrial operations but, at the same time, induced earthquakes are also a required mechanism to increase the permeability of rocks, enhancing reservoir performances. For these reasons in urbanized areas deep geothermal resources can only be exploited if the problem of controlling induced seismicity is adequately addressed. The failure of recent projects such as Basel (2006, Switzerland), St Gallen (2013, Switzerland) and Pohang (2017, South Korea) highlighted that existing tools for seismic hazard management in hydrocarbon and geothermal reservoirs (the so-called "Traffic Light System" TLS - e.g., Bommer et al., 2006; Haering et al., 2009; Bosman et al., 2016) are not sufficient to warrant the safety of such industrial operations. TLSs are based on or several decision variables, typically three main observables: 1) public response, 2) observed local magnitude and 3) peak ground velocity and acceleration. In a four-stage action plan, the injection of fluids would either be 1) continued as planned (green); 2) continued but not increased (yellow); 3) stopped (orange) or 4) stopped and a "bleed-off" initiated (red). So far, TLSs do not take in consideration the full range of possible scenarios and the uncertainty of the process. As they have no capability to forecast the seismicity produced by a specific

injection protocol, they resulted ineffective in preventing felt induced earthquakes that led to the definitive closure of several projects around the world. Hence, to mitigate the overall risk more advanced tools and workflows are required.

In this context, one of the main aims of DESTRESS is to provide operators with a reliable decision tool to estimate the risk of induced seismicity following reservoir operations. Such tools are referred to as Adaptive Traffic Light Systems (ATLS) and were spearheaded in the EC project GEISER.

ATLS are decision support tools that are fully probabilistic, data-driven (in the sense that microseismic date are integrated in real-time to update geomechanical and seismicity forecasting models) and risk-based (integrating hazard, exposure, and vulnerability). The technical diagram describing the workflow of the ATLS is shows in **Figure 1**.

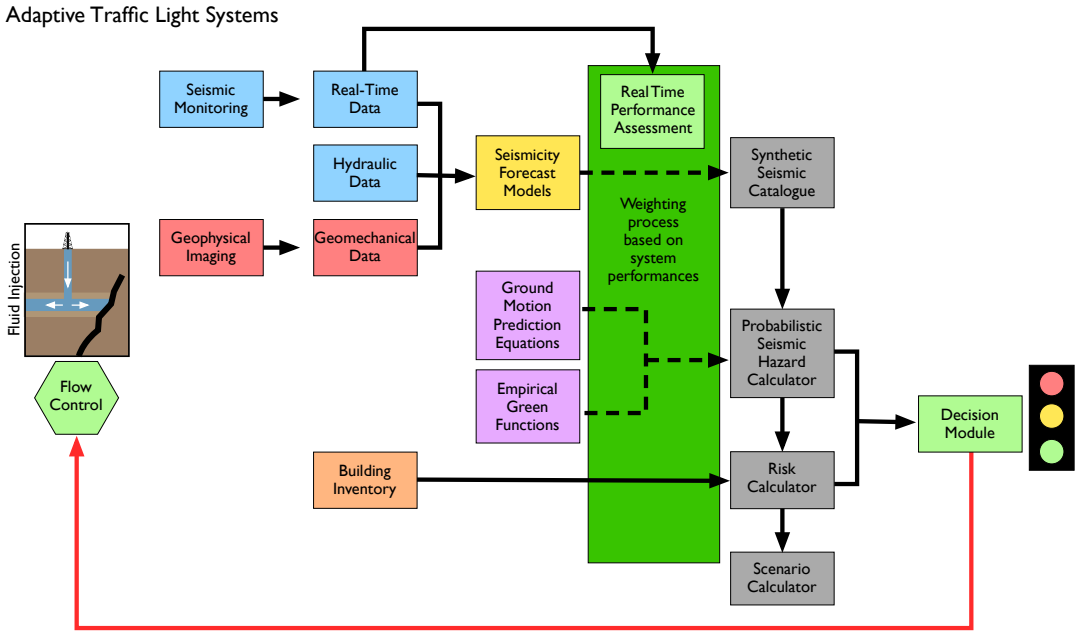

Figure 1: Schematic representation showing the workflow of the ATLS.

They are designed to overcome the limitations of the traditional heuristic methods. Here, the assignment of a magnitude threshold is based on a quantitative risk assessment, subject to a safety criterion imposed by the authorities (e.g., fixed probabilities of unaccepted nuisance, damage or fatalities). As a consequence, the ATLS is an objective and statistically robust mitigation strategy, which facilitates a fair and transparent regulatory process. This approach is in line with the procedures common for most other technological risks, such as in the hydropower, nuclear or chemical industries. Model-based forecasting and alerting are already advocated elsewhere, such as in hurricane data assimilation and forecasting. ATLS are fully probabilistic, data-driven (in the sense that new data is integrated on the fly to update geomechanical and seismicity forecasting models) and risk-based tools that integrate all relevant information, such as hazard, exposure, and vulnerability of the structures close the industrial sites. In the next section we will describe in more detail the characteristics of Advanced Traffic Light Systems, which consists in its simplest form of two main components:

- **Induced Seismicity Monitoring Tool**
- **Seismicity Forecasting and Risk Analysis Tool**

II. Induced Seismicity Monitoring Tool

One of the major challenge in ATLS concept is the ability to detect and locate micro-earthquakes reliable, accurately and in a highly automated way, down to the smallest possible magnitude. We also need to determine source parameters (magnitudes, stress drops, focal mechanism). In the concept of the EU project DESTRESS, we evaluated the capability of Distributed Acousting Sensing (DAS) systems in monitoring microseismicity and developed an improved workflow for highly automated seismological data processing, fully integrated into the open-source software framework SEISCOMP3. The goal of these developments is to greatly improve the baseline seismological data that is the input for real-time seismicity forecasting and risk assessment.

Microseismic Monitoring Infrastructures

Microseismic monitoring is the fundamental tool used by decision makers to decide, whether to stop, decrease or continue the industrial operations being monitored. High density microseismic monitoring networks allow the detection of weak events (generally below magnitude 0), even in presence of strong noise contamination. For this reason, a high-quality monitoring network should be combined with noise robust, real-time and fully automated data analysis procedures, which are required to handle large datasets (Cesca and Grigoli 2015).

To ensure an optimal monitoring of induced seismicity two main conditions should be satisfied: 1) the use of high quality microseismic monitoring networks based on leading edge technologies and 2) the use of sophisticated near real-time data analysis procedures.

DAS monitoring systems are recognized as serious alternative for traditional seismic monitoring systems and their capabilities for monitoring of microseismic events have been demonstrated recently. DAS has the main advantages that it can acquire reliable data, with a high spatio-temporal resolution at a relatively low-cost. Moreover, recent studies have shown that pre-existing telecom cables can be potentially used to record seismicity further favoring this technique as a low-cost alternative for conventional (micro)seismic monitoring systems (Lindsey et al., 2017; Jousset et al., 2018). Numerical simulations can help to test the capability of using DAS fibre-optic sensing for (micro)-seismic monitoring. Based on outcomes from literature concerning DAS studies, representative operational parameters, such as geometry and signal-to-noise ratios, can be adopted into simulations.

In general, the completeness of earthquake catalogue data relies on the availability of reliable monitoring data, such that relevant earthquake characteristics can be determined accurately. Various literature sources provide monitoring recommendations specifically for geothermal sites (Baisch et al., 2016; Bohnhoff et al., 2018; Kraaijpoel et al., 2013; Majer et al., 2012), where a minimum detection level for PGV at the surface of 2*10-5 m/s is recommended. For a representative geothermal site this roughly corresponds to an M~0 earthquake, whereby actual detected signal strength is also determined by elastic medium properties and seismic survey geometry. Maximum noise amplitudes on the order of 2*10-6 m/s in the range 5-40 Hz are recommended by Kraaijpoel et al. (2013). Recently various studies demonstrate the added value of using distributed acoustic sensing systems (DAS) within seismic monitoring networks (Mestayer et al., 2012; Mateeva et al., 2014). The signal obtained from such systems is a distributed measurement over a length of cable defined as the gauge length (see **Figure 2**). Using optical interferometry, strain within the fibre is measured down to micrometer level and up to 1000 Hz. The gauge length, approximately corresponding with spatial sensor-recording interval in conventional point sensor recording, is in the order of 1-10 meter. A total fibre optic length of 10 km is available for recording and thus up to +- 10000 channels can be effectively used. Recording bandwidth is 1- 1000 Hz which is considered broadband in seismic acquisition. Currently, quite some conventional seismic acquisition systems exist with similar specs, but what really sets DAS apart is where and when it can record. The measuring string of DAS is merely a fibre optic cable, whereas conventional geophone systems have bulky sensors, cables and boxes. WiFi solutions exist but are not suitable around metal casing. Most important: DAS fibres can access locations and under conditions that are out of reach for conventional geophones. A DAS fibre can be mounted outside the casing, in the cement or even outside the cement for direct contact with the reservoir. The fibre can withstand

high overpressures and temperatures, up to 100 bar and 250° C. These systems could provide additional information within a network of standardized seismometers. An important aspect of DAS systems is whether they meet the requirements necessary to feed a traffic light system with reliable seismicity information. The sensitivity of DAS systems should be sufficient to reach desired or required minimum magnitude and PGV values as well as acceptable even location accuracies.

In the work presented here, we approximate synthetic noise levels by adopting typical DAS noise levels from literature in which earthquake events were analyzed within real DAS data (Lumens, 2014; Lindsey et al., 2017). These noise levels can be considered as the bulk effect of the four categories of transfer functions. Note however that these noise levels are of course site specific and dependent on the geology, well design, design of the DAS cable and type of interrogator. Lindsey et al. (2017) compared the earthquake response of a DAS cable buried in a shallow trench to a seismometer recording in Central Alaska for an M3.8 event. Lumens (2014) considers DAS noise levels in Oman for weak earthquakes on the order of M~0.

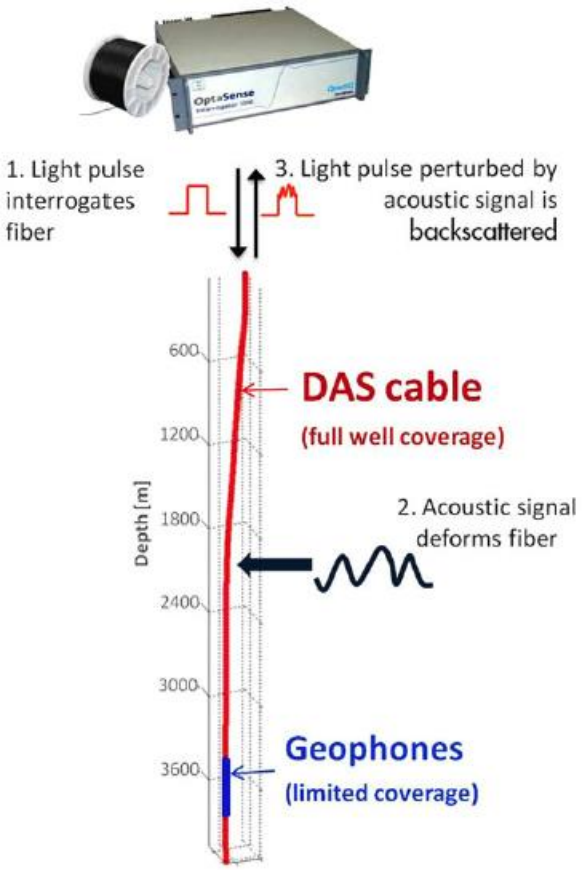

Figure 2: Schematic presentation of VSP recording with DAS (from Mateeva et al., 2014).

In our simulation we considered a site in the Netherlands where geothermal operations are planned, situated near Utrecht. Here the Rotliegend sandstone is the anticipated reservoir and situated at approximately 1750 m depth. Velocity information from a sonic log in the vicinity of the anticipated geothermal site, was used to construct a P-wave velocity model (well Jut-01 obtained from www.dinoloket.nl). S-wave velocity models were estimated from Castagna relationships (Castagna et al., 1985). The seismic wave propagation modelling package SPECFEM2D was used to conduct forward simulations (Komatitsch and Tromp, 1999; Tromp et al. 2008). SPECFEM, of which SPECFEM2D forms a module, relies on the spectral element method and is an efficient package for calculating elastic simulations, thereby accommodating complex velocity structures. The geometry of the SPECFEM model used here is shown in **Figure 3**. Several simulations were conducted to address the effect of attenuation and of different noise conditions on DAS data.

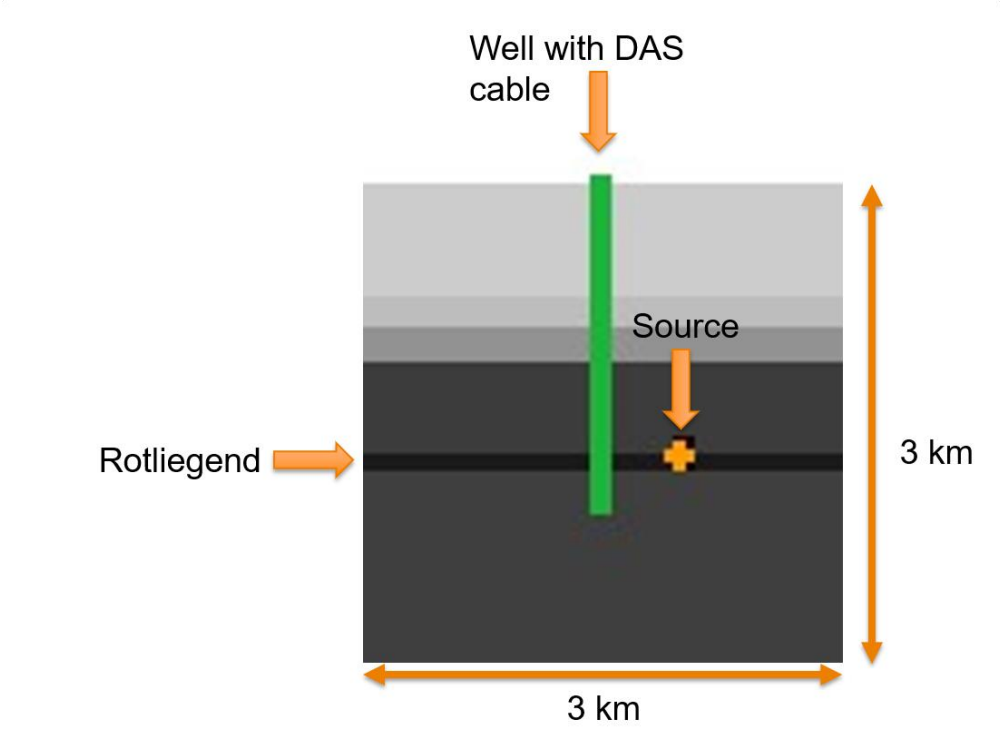

Figure 3: Geometry of the SPECFEM2D model.

Simulations of elastic wave propagation were conducted resulting in synthetic ground motion recordings along the synthetic DAS line. As a first order approximation we address the DAS directivity by only considering the vertical component of the simulated data, since the DAS response is maximum parallel to the fibre direction, which is vertical in our case. **Figure 4** shows snapshots of the vertical velocity component of the wavefield for 6 successive times. Synthetic DAS receiver panels calculated during the simulation are shown in **Figure 5**, that include attenuation prescribed by the quality factor (Q), where we perturbed the synthetics with gaussian distributed noise. Here the SNR is calculated on the full time window of the synthetic waveform and defined by:

$$SNR = \frac{\max(abs(signal))}{\max(abs(noise))} \qquad (1)$$

Figure 5a shows the vertical component receiver gather that is unperturbed with noise, whereas **Figure 5**b and c respectively have SNR levels of 10 and 2. The increasing perturbation of the signal with noise illustrates how the signal will eventually be masked by the background noise level.

In **Figure 6**a, a comparison is made for the peak differential displacement calculated over 10 m gauge lengths. The result is compared against the noise floor observed for DAS recordings by Lumens (2014). This shows that for the considered simulated earthquake within the elastic medium we prescribed the synthetic displacements exceed the DAS noise level by far, thus having a sufficiently high SNR. **Figure 6**b shows the comparison of peak differential displacement versus depth with a comparison to the lower detection threshold recommended for traffic light systems (Kraaijpoel et al., 2013). This shows that for the entire depth range the DAS response is sufficient to detect the considered simulated event, as it falls above the noise level. **Figure 6** also shows significant variations in depth of peak displacement- and velocity values, due to partial transmission and reflection of the propagating wavefield at elastic contrasts and the effect of the angle of incidence; note that we only consider the vertical component here. The noise conditions will be further addressed more carefully based on literature to address whether the performance of DAS is expected to be sufficient for detection of weak seismic events.

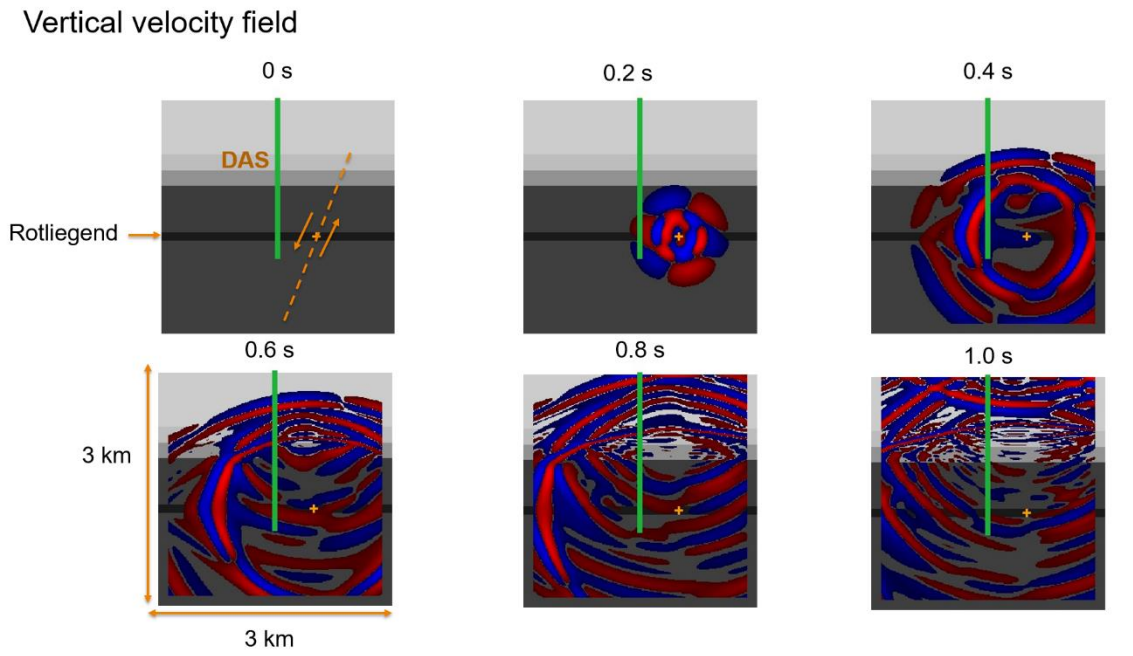

Figure 4: Snapshots of elastic wave propagation of vertical particle velocity field.

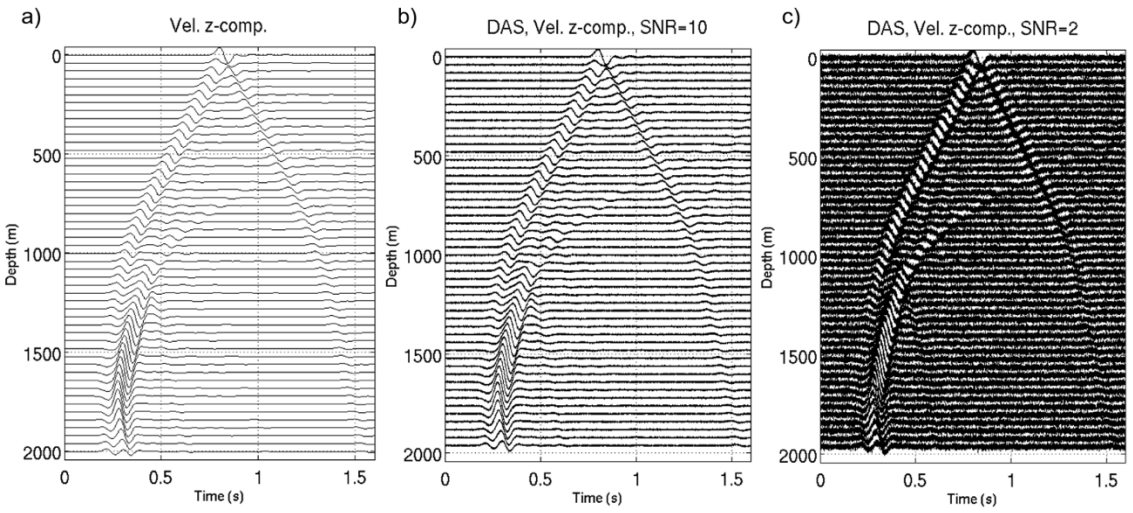

Figure 5: Synthetic vertical component data for various noise conditions with attenuation (Q=50). A) No noise. B) Gaussian distributed noise with SNR=10. C) Gaussian distributed noise with SNR=2. Note in this figure a vertical trace spacing of 40 m was used to improve visibility, although the actual synthetic trace spacing was 2 m.

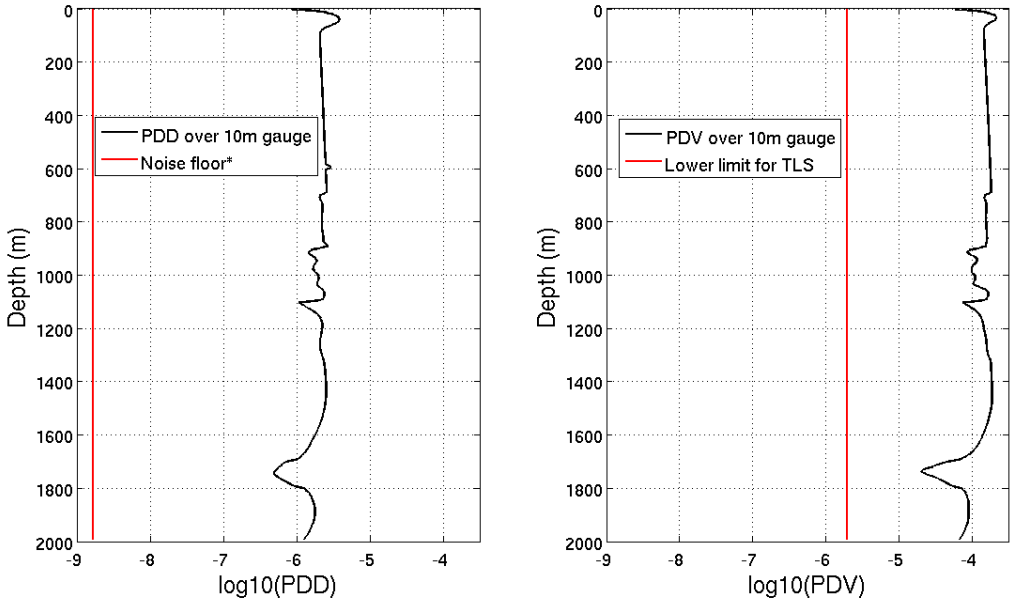

Figure 6: a) Peak differential displacement (PDD, black) calculated over 10 m gauge length versus depth for the simulated data shown in **Figure 4**a. The DAS noise floor from Lumens (2014) in red, is 2-3 orders of magnitude below the peak differential displacement for the entire depth range for the considered simulated earthquake event. a) Peak differential velocity (PDV, black) for 10 m gauge length together with lower detection threshold limit recommended for traffic light systems (red, Kraaijpoel et al., 2013). The peak differential velocity falls above the detection threshold for the entire depth range.

Within the project DESTRESS we prepared and tested a modeling approach to simulate the DAS response with SPECFEM2D. The approach is ready for use in more realistic scenarios. Here one can consider various site-specific conditions determined by well design, DAS cable design, type of interrogator and local geology. Based on initial results we expect that DAS can be suited to feed traffic light systems in the near-future, given the ongoing improvements in placement and performance of these systems. To reach sufficient spatial coverage to monitor a geothermal reservoir, it is likely that additional surface seismometers are required in addition to a DAS cable deployed along the well. This will be required to allow localization of seismic events with sufficient accuracy, especially further away from the well. Alternatively, a DAS cable could be deployed in a near-surface trench.

The desired performance on detection and location of an induced seismicity monitoring infrastructure is strongly dependent on the type of application (Trutnevyte and Wiemer 2017) and should be designed in synergy with a risk assessment and site characterization phase, for the cost-benefit optimization. The accuracy of the location performance is important to understand ongoing seismic processes (e.g., to map the spatio-temporal evolution of the seismicity which could reflect fluid migrations)(Ogwari et al. 2016), but also is a fundamental information to discriminate between natural and induced seismicity (Dahm et al. 2013). However, also in this case, the desirable location uncertainty remains intrinsically linked to the type of operations and potential hazard. Since the location performance is not only controlled by the geometry and technology of the monitoring infrastructure, but also on the adopted methodology for location and on the available velocity model, tests with synthetic simulation and real data remain the best practice to assess the location performance of the network (Kinnaert et al. 2016). Location uncertainties can be reduced by using dense networks with at least one station (better if deployed in a borehole) directly above or within few kilometers from the potential source of seismicity (e.g. injection well).

In order to efficiently monitor induced microseismicity, well designed monitoring networks using leading edge technologies need to be combined with advanced data analysis methods. We thus need efficient real-time earthquake detectors, high precision locations and reliable source parameters (e.g.

magnitude and, if possible, source mechanisms). Since microseismic events are often characterized by low signal-to-noise ratio, obtaining reliable source parameters is still challenging (Cesca and Grigoli 2015). In addition, microseismic networks generally record a large number of weak earthquakes (magnitude completeness of these networks is commonly Mc<=0.0), and quick analysis of such huge datasets is hardly achieved through manual data analysis procedures. Thus, robust automated data analysis procedures should be established.

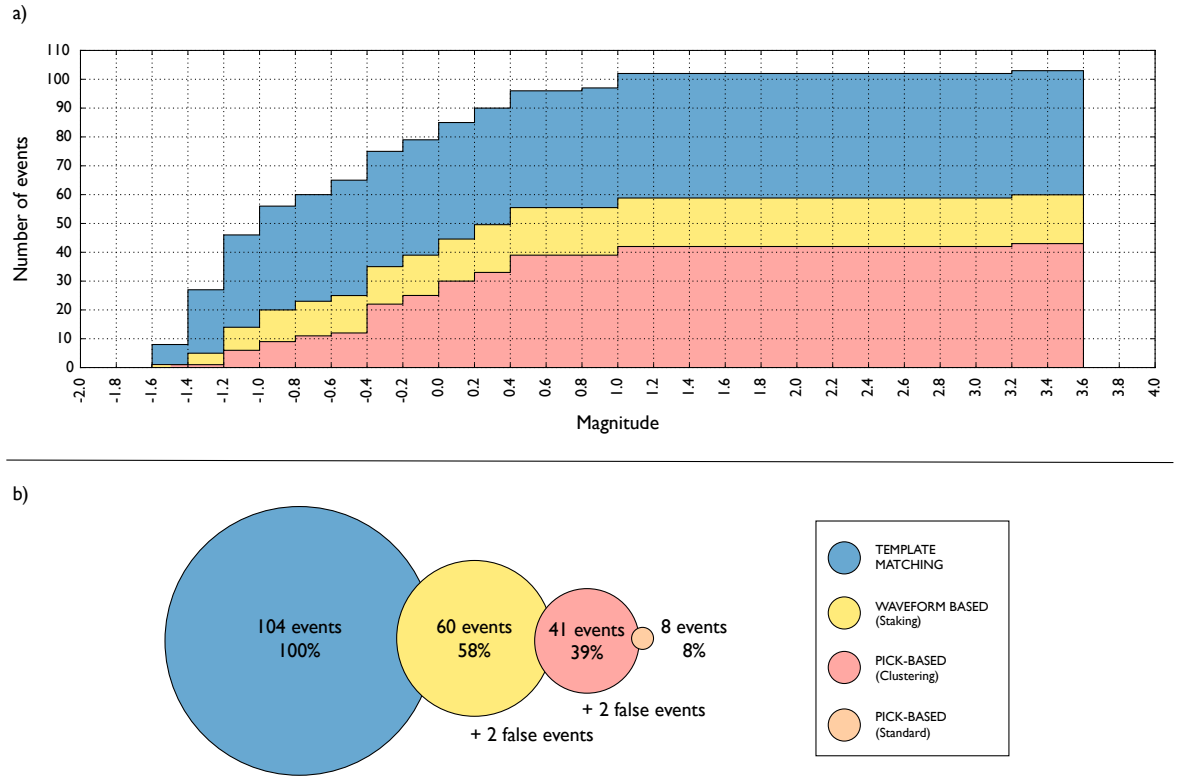

Figure 7: Summary of detection results for the first hour of the Mw 3.3 St. Gallen Seismic Sequence. (a) Cumulative plot showing the number of events detected by each method as a function of magnitude. (b) Total number of detected events. Each colour represents a different detection method. (from Grigoli et al. 2018)

Modern methods can be used as robust and fully automated procedures for microseismic data analysis, which can lead to more reliable results than standard approaches. Among these approaches, detection methods based on waveform template matching have been extensively applied to induced seismicity datasets (Skoumal et al. 2015, Yoon et al. 2015). Within DESTRESS we developed new seismological analysis techniques and we applied them to the St. Gallen induced seismicity sequence (Grigoli et al 2018). Finally, we compared the results with those obtained by using standard analysis techniques. As illustrated in **Figure 7** waveform template matching allows successful detection of a large number of hidden events which often are buried by noise and lead to a dramatic increase of the catalog completeness, highlighting more detailed relationships in the space-time-magnitude domain between the seismicity and industrial activities (Skoumal et al. 2015, Bao and Eaton 2016, Goebel et al. 2016). However, these approaches need a high-quality reference catalogue which need to be obtained with other techniques. Also in this case new detection and location techniques over perform the standard seismological analysis techniques. The **Figure 7** shows in fact that standard approaches only detect 8% of the total seismic events.

It is also important to point out that the performance of absolute location methods strongly depends on the quality of the available velocity model. When dealing with poor velocity models location

accuracy can be strongly reduced, affecting the output of further geological and geophysical analysis (e.g. estimation of source mechanism, event magnitude, etc.) (Grigoli et al 2016). To reduce the dependence on the velocity model and obtain more accurate results, relative location methods are thus required. Most of these methods rely on differential travel times for pairs of earthquakes observed at common stations (Waldhauser and Ellsworth 2000), which can be computed automatically using cross-correlation (Schaff and Waldauser 2005). Differential times can be now computed in a fast and efficient way, allowing to obtain double difference locations in real-time (Waldhauser and Schaff 2008). The Real-Time Double-Difference analysis has been successfully applied to the northern California seismicity, including induced seismicity recorded at the Geyser geothermal field (Waldhauser 2009) (http://ddrt.ldeo.columbia.edu). Within DESTRESS we developed a new open-source Seiscomp3 module that performs relative seismic event location using the Double-Difference approach in real-time (scRTDD).

Robust magnitude estimation is also important and should be performed in any induced seismicity monitoring operation. The quality of the magnitude estimation, as for the location, will depend also on the monitoring setup. In this perspective, the presence of one or more broadband seismometer remains fundamental to cover low frequency (i.e. less than 1 Hz) spectra and to better constrain the magnitude of larger events, which can, in combination with a short period seismic network, be used to calibrate magnitudes of smaller earthquakes. Given the multiple magnitude types and estimation techniques, transparent procedures to estimate the magnitude should be provided. The magnitude determination is not a trivial process, and important differences have been detected among different catalogs related to induced seismicity (Edwards and Douglas 2014). Moreover, induced seismicity often occurs in low seismicity region, where robust attenuation curves cannot be easily calibrated. Weak induced events (i.e. generally with magnitude less than 1) may be recorded only locally and the adoption of regional attenuation laws may bias the magnitude estimation. The problem has been recently illustrated for the Blackpool (UK), induced seismicity case by (Butcher et al. 2016), who depicted large, critical discrepancies between magnitudes calculated using local-distance stations (Ml 2.3) and those based on records from the regional network (Ml 1.2). This has obvious significant implications for the regulation of the risk of induced seismicity, which is often managed on the base of traffic light schemes, depending on the estimated magnitude. The radiation pattern of earthquakes can affect magnitudes, e.g. if the monitoring network has large azimuthal gaps. Therefore, full waveform modeling techniques to characterize the seismic source processes are useful to investigate the geometry of active faults, to detect tensile failures or to investigate stress drops. These techniques also benefit from the availability of broadband records, possibly covering the source radiation patterns from different azimuths (Grigoli et al. 2017).

Finally, it is worth to highlight that a good microseismic network is a necessary, but not sufficient condition to successfully monitor induced seismicity. Although several advanced and reliable analysis methods are currently available, in routine monitoring operations most of the processing is done using standard approaches which often do not lead to reliable results when dealing with noisy data or when the velocity model is poorly known. In many cases, in fact, routinely monitoring operations are performed by using techniques not specifically designed for this type of applications, thus they may not fully exploit the performance of the monitoring infrastructure. Within DESTRESS we have shown that the combination of optimal network infrastructures with sophisticate data analysis techniques lead to better seismic catalogues which are main input for current ATLS systems, strongly helping in the decisional process during crises.

III. Seismicity Forecasting and Risk Analysis Tool

Planning phase, preliminary hazard and risk analysis

A seismic risk assessment is generally requested by authorities before a new project can be accepted. An example of a risk report for a Swiss DGE project can be found online:

Synthèse des études relatives à la sismicité induite, Projet pilote de géothermie profonde Haute-Sorne, by Geo Energie Suisse (on https://www.jura.ch/)

Here we will present an example workflow for the site of Haute-Sorne. Note that that analysis here is an example with realistic but somewhat arbitrary assumptions, intended to illustrate the principle workflow and sensitivities. It is not identical to the official risk assessment conducted by the operator and judged by the cantonal authorities, and it is not an official assessment of the Swiss Seismological Service.

T A project can often start with a pre-screening as suggested by Trutnevyte and Wiemer (2017). A risk assessment includes a regional study of the tectonics, natural seismicity, and built environment. It describes the injection protocol and how induced seismicity would be evaluated (by seismic monitoring - see previous section about monitoring) and mitigated (classic TLS with magnitude threshold or vibration threshold following various norms - see next section for an alternative). Various risk scenarios (deterministic and probabilistic) are described (see also Mignan et al., 2015 and the Haute-Sorne case below). The possibility of a large earthquake (above the McGarr limit) is also investigated by fault mapping (cartography, geomorphology, seismic reflection) and physical modelling (by using standard approaches such as stress transfer computations). Distinction is often made between the following phases: planning, drilling/logging/testing, stimulation, operation, and post-operation. For a proposed detailed structure of the risk report (introduction and context, project description, hazard and risk assessment, proposed monitoring and mitigation strategies, summary and recommendations), see SED (2017).

In the planning phase, we advise a preliminary probabilistic induced-seismic hazard and risk analysis. It is important to remark that in this phase the goal is to determine a first-order earthquake-induced hazard and its propagation to the risk assessment. As such, the immediate aim is to provide a preliminary baseline for operators and stakeholders for a coherent decision making, communication and mitigation actions. Therefore, the preliminary assessment is suitable for the planning phase and on the long term, updates and revisions are expected after interactions with the operators and stakeholders.

In a probabilistic setting, the study should follow the standard definition of the seismic risk as the convolution of three components: hazard, vulnerability, and exposure. We can summarize the analysis in the following key points:

- Definition and selection of the sources of epistemic and aleatory variability
- Definition and selection of the earthquake source and rate models
- Selection of the reference intensity measure and selection and/or definition of ground motions predictive equations (GMPEs) and the intensity predictive equations (IPEs)
- Definition and selection of vulnerability function and related consequence models based on the exposure asset of the region
- Organization of the selected different models into a logic tree structure

The output of the analysis is a preliminary probabilistically characterization of the potential financial losses for each settlement of interest, and/or aggregate for the entire built portfolio. In addition, when variability of the output is large, we recommend a sensitivity analysis to determine the contribution of each parameter to the variability of the estimated financial losses. The detailed analysis should be organized as follows: the first part presents the input datasets and models and the logic tree structure,

the second part shows details of model implementations, and end-to-end calculation of the fluid-induced seismic hazard to risk; the third section (optional) presents a sensitivity analysis to understand the driving variables defining the seismic risk. In this document, we report general suggestions for implementation details. However, deviations from what we report are possible and, sometimes, recommendable if a more detailed solutions are available.

Preliminary Seismic Hazard analysis

For a preliminary assessment, we suggest to use the classical Probabilistic Seismic Hazard Analysis (PSHA) (Cornell, 1968; McGuire, 1995) adapted to account for the time variant rate of seismicity (typical of induced seismicity). There are two key elements in PSHA: (a) the definition and the probabilistic characterization of the seismogenic source model, and (b) the ground motion characteristic model describing the expected ground shaking given the occurrence of an earthquake. The first provides the spatial and the temporal forecast of the earthquake ruptures, whereas the second links the earthquake rupture with the expected ground shaking at the site of interest (via the GMPEs). The outputs of PSHA are either rate of exceedance or hazard curves (probability of exceedance for a given period of time) of a selected ground shaking Intensity Measure type (IM), such as peak ground acceleration (PGA), velocity (PGV), spectral acceleration (SA) and/or macroseismic intensity.

To include also the epistemic uncertainties, given the alternative interpretation of data, assumptions and decisions (i.e. selection of the appropriate physical and statistical models) a logic tree structure with weighted branches (representing the belief of a given model) must be defined. **Figure 8** shows an example of a schematic logic tree. The first level of the logic tree describes the uncertainty related to the selection of the rate model, while the second level on the uncertainty relates to M_{max}, the third level the GMPE&GMICE level, the fourth level the vulnerability models, the final level the cost functions. This scheme has been adopted in Mignan et al. 2015 and Broccardo et al. 2019 (in preparation).

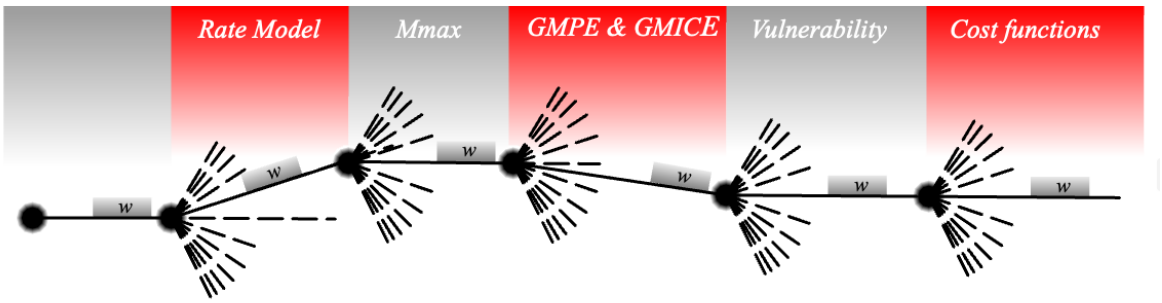

Figure 8: Logic tree scheme for a preliminary hazard and risk analysis

In a preliminary investigation, it is acceptable to assume that the induced earthquakes nucleate and eventually extend in the proximity of the injection point. Consequently, a point source located at the coordinates of the injection point can be adopted as the unique source model. However, this implicitly excludes any geometrical uncertainty on the hypocenter location.

A characteristic that differentiates fluid-induced seismicity from natural seismicity is the time- variant rate of seismic events. In fact, it has been shown by several studies (Mignan et al., 2017; Broccardo et al., 2017; Ellsworth, 2013; Langenbruch et al., 2011; Shapiro and Dinske, 2009), that this is related to the rate of the injected fluid. Consequently, while a homogeneous Poisson Process is appropriate for natural seismicity (which is characterized by constant base rate λ_0), fluid-induced seismicity, generally (with some exceptions), follows a Non-Homogeneous Poisson Process (NHPP) with a given time-variant rate $\lambda(t)$. The true rate $\lambda(t)$ is not known a priori, and it can be estimated either with a computational model, or with an empirical relationship (or both). Specifically, we recommend the relationship $\lambda(t) =$

$10^{a-bm_0}\dot{V}(t)$ with $\dot{V}(t)$ being the rate of injection of the fluids during the stimulation, and m_0 the magnitude of completeness. This empirical linear relationship between number of earthquakes and volume injected is well accepted in the seismological community (Dinske and Shapiro, 2013; Mignan, 2016; van der Elst et al., 2016; Mignan et al., 2017; Broccardo et al., 2017b). Note that it only applies to the stimulation phase in which the fluids injected are not supposed to be back produced, hence creating an overpressure field at depth *z*. The validity of the model is illustrated on **Figure 9** for some high-quality induced seismicity data. While the underground feedback parameters *a* (i.e. the overall activity for a given volume *V* injected somewhere) and *b* (i.e. the ratio between small and large earthquakes) can be estimated during the stimulation (Mignan et al., 2017; Broccardo et al., 2017b; see next section), *a priori* knowledge on those parameters is limited and the range of possible values wide. We list parameter estimates for different sites in **Table 1**.

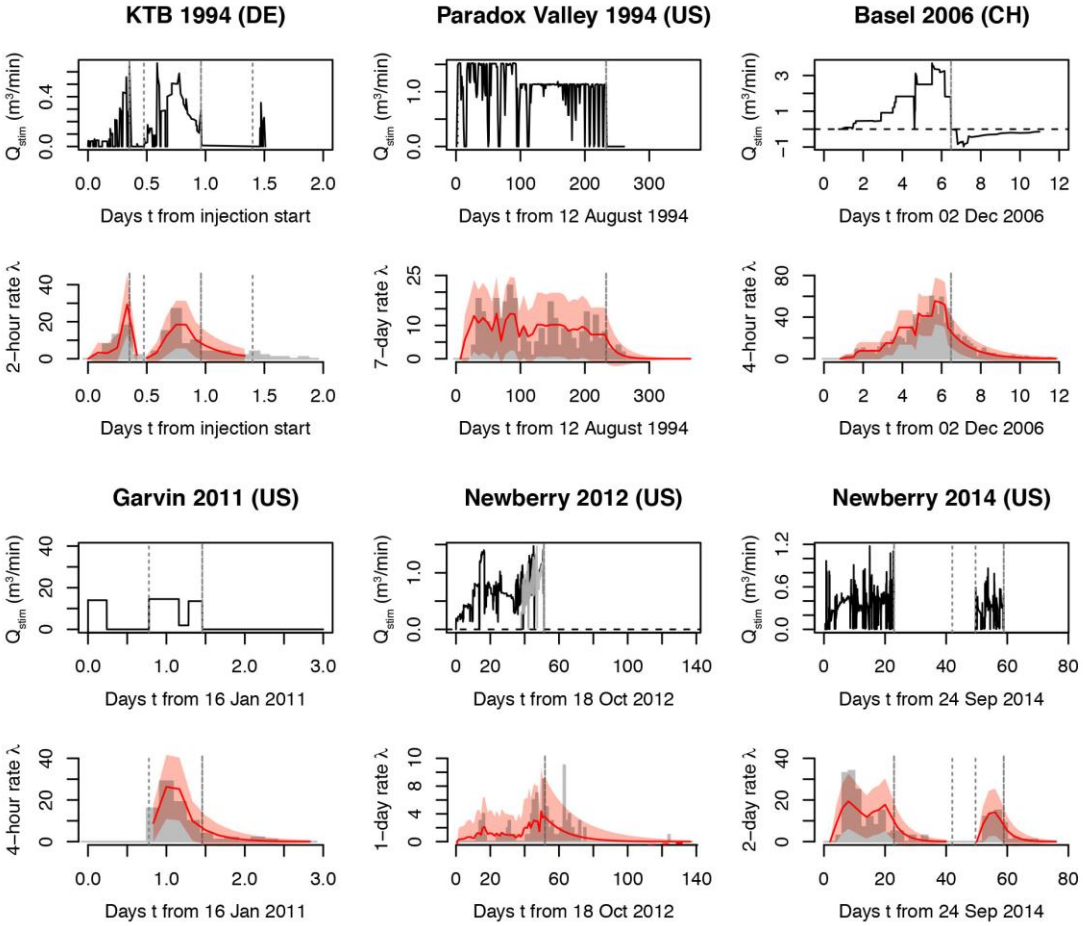

Figure 9: Induced seismicity model fitting of six (high-quality data) fluid injection experiments. The observed seismicity rates are represented in grey and the model (i.e., the linear relationship between stimulation flow rate Q_{stim} and seismicity rate) in red.

Table 1: Underground seismic feedback to deep fluid injection.

Site (country*, year)	*a*†	*b*	References
Ogachi (JP, 1991)	-2.6	0.7	Dinske and Shapiro (2013)
Ogachi (JP, 1993)	-3.2	0.8	Dinske and Shapiro (2013)
Soultz (FR, 1993)	-2.0	1.4	Dinske and Shapiro (2013)
KTB (DE, 1994)	-1.4	0.9	Mignan et al. (2017)
Paradox Valley (US, 1994)	-2.4	1.1	Mignan et al. (2017)
Soultz (FR, 1995)	-3.8	2.2	Dinske and Shapiro (2013)
Soultz (FR, 1996)	-3.1	1.8	Dinske and Shapiro (2013)
Soultz (FR, 2000)	-0.5	1.1	Dinske and Shapiro (2013)
Cooper Basin (AU, 2003)	-0.9	0.8	Dinske and Shapiro (2013)
Basel (CH, 2006)	0.1	1.6	Mignan et al. (2017)
KTB (DE, 2004-5)	-4.2	1.1	Dinske and Shapiro (2013)
Newberry (US, 2012)	-2.8	0.8	Mignan et al. (2017)
Newberry (US, 2014)	-1.6	1.0	Mignan et al. (2017)

* ISO code; † referred to as seismogenic index in Dinske and Shapiro (2013).

In the preliminary hazard analysis, to facilitate standard hazard computations, we suggest to convert the time-variant rate into an equivalent stationary rate, i.e. $\bar{\lambda} = \int_0^{\mathrm{T}} \lambda(\mathrm{t})\,/\mathrm{T}$ (where T is the total duration of the project). As a consequence, the classical Homogeneous Poisson Process (HPP), and the classical probabilistic seismic hazard analysis (PSHA) can be used to define the occurrence model of the induced earthquakes. By using the proposed empirical model the "homogenized" $\bar{\lambda} = 10^{a-bm_0}\mathrm{V}/T$ can be defined directly by the total volume of the injection, which is known a-priori.

The frequency magnitude distribution, has been proved to follow the classical Guttenberg-Richter distribution. However, one of the major source of uncertainty and debate is related to the upper bound of the (truncated) Guttenberg-Richter distribution. The debate is closely related to the above reported dispute between induced versus triggered seismicity. Since the complete information about the number, location, and stress condition of all active faults in the area of injection cannot be available (in particular before the stimulation phase), it is appropriate to consider both M_{max}s of induced and triggered seismicity. Specifically, the first ones are bounded by McGarr (1976, 2014) upper limit (which is based on the volume affected by the fluid pressures), while the second ones are bounded by the tectonic M_{max}). Consequently, covering in the logic tree the tectonic M_{max} is generally a conservative and strongly recommendable approach in a preliminary fluid-induced hazard and risk analysis. Soil amplification factors, uniform or based on micro-zonation should be included if available.

In the preliminary assessment, we suggest to use as IM the European Macroseismic Scale (EMS98, Grünthal, 1998). The advantage of EMS98 over these IMs in a preliminary phase lies in the easier interpretability of this scale, which is based merely on shaking indicators expressed in terms of damage and nuisance to the population. Based on this considerations, when the selected GMPEs are expressed in terms of peak ground acceleration, peak ground velocity, or other ground intensity measure they should be converted into expected intensity by using a Ground Motion to Intensity Conversion Equation (GMICE) for small-medium intensities (e.g. Faccioli and Cauzzi, 2006, Faenza and Michelini 2010).

Once the logic tree is completely defined by the rate models, the M_{max}s, the GMPE & GMICE combinations, the hazard computation is given by classical convolution of all source of uncertainties for each branch of the defined logic tree. The output of analysis are the so-named hazard curves, i.e.

probability of exceedance of a given intensity measure normalized to one injection period, for each location of interest. Together with the hazard curves, we recommend also to provide Hazard maps, for a given probability of exceedance with respect to the median of the hazard curves. **Figure 10** shows an example of hazard map for a probability of exceedance of the median hazard curve of $P(IM > im; T) = 10^{-4}$, together with the Hazard curves for a given site of interest. The reference project is the Haute-Sorne Enhanced Geothermal System project.

Preliminary Seismic Risk analysis

Seismic risk is computed by convolving a vulnerability models for the relevant building typologies with the exposure model. In a preliminary risk analysis, we recommend to use a vulnerability given in terms of macroseismic intensity, which follows the macroseismic approach for damage assessment (Baisch et al., 2009; Lagomarsino and Giovinazzi, 2006) and that was modified in Mignan et al., 2015 for the induced seismicity case. In this approach, the vulnerability is not defined based on detailed mechanical models; therefore, it is implicitly assumed that macroseismic and mechanical approaches produce compatible levels of damage.

The macroseismic model defines the mean damage grade, $\mu_D(im)$, as function of a vulnerability index V, a ductility index, Q, and a reduction factor α introduced in Mignan et al. (2015) to recalibrate low damage states to the damage observed in the Basel 2006 sequence. The vulnerability index depends on the building class and construction specifics, and it includes (Lagomarsino and Giovinazzi, 2006) probable ranges $V-V+$, as well as less probable ranges $V--V++$. In case no information are available on the vulnerability index range, it is recommendable to use V_0 in a preliminary phase. Moreover, is no datelined information is given on the ductility index for the different class of building, we recommend to use $Q = 2.3$, which is the value for masonry structures and reinforced concrete structure with no seismic details. In this phase, this a practical and conservative choice because $Q = 2.3$ is a lower bound of the possible ranges of values for the ductility index. **Figure 11** shows the fragility functions obtained by using the macroseismic model with parameters $V_0 = 0.74$, and $Q = 2.3$.

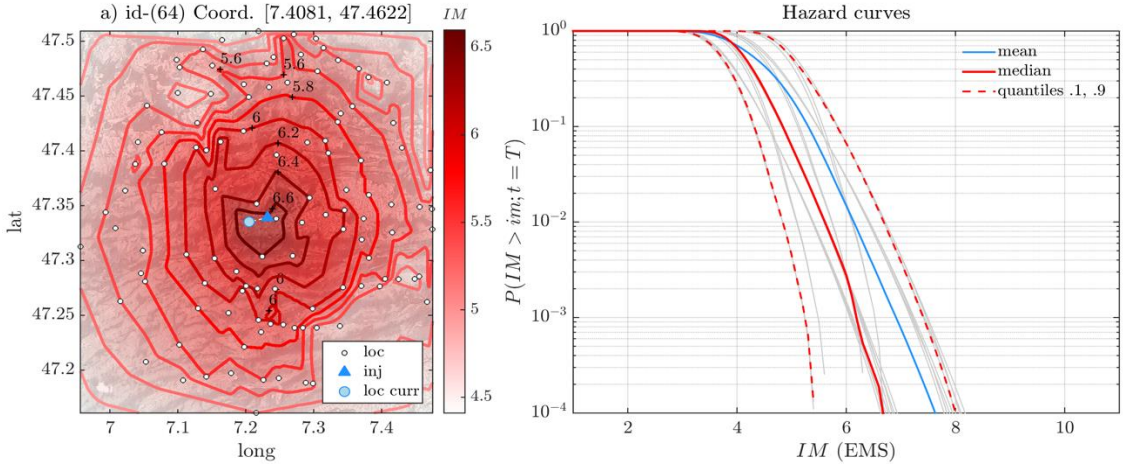

Figure 10: a) Hazard map for the region of interest, based on the the $q_{10^{-4}}$ of the median. Units: EMS b) Hazard curves for the site of interest. Source: Broccardo et al. 2019 in preparation.

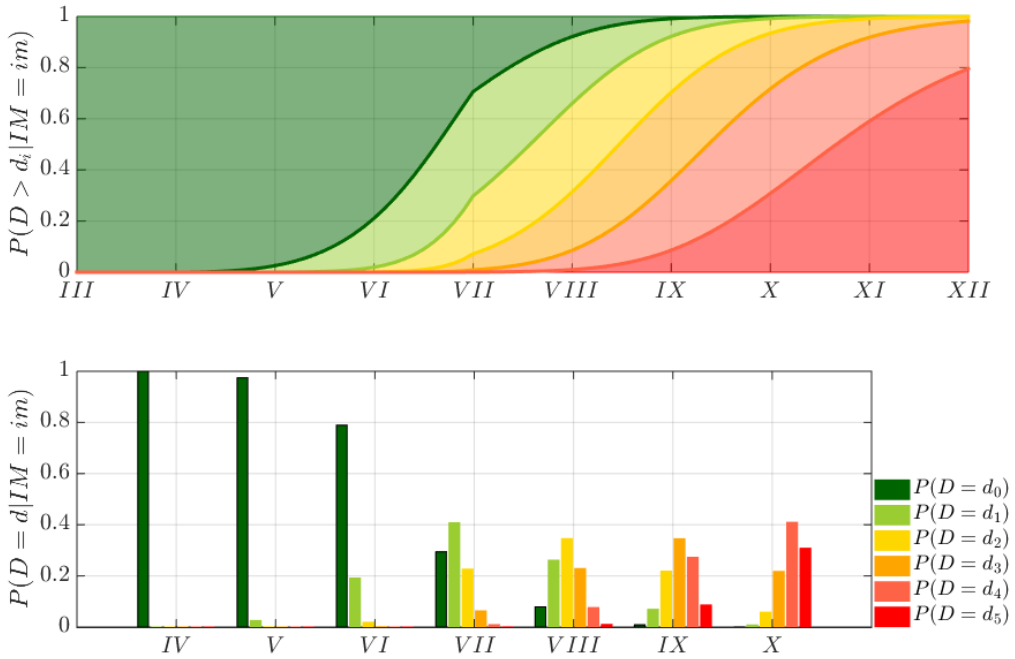

Figure 11: Top subplot: fragility functions, bottom subplot: probability mass function $\mathrm{p_D(d_k)}$ for different level of intensity. The discontinuity at $\mathrm{im = VII}$ is due to correction faction $\mathrm{\alpha(im)}$ introduced in Mignan et al. (2015). Source: Broccardo et al. 2019 in preparation.

Damage assessment is translated directly into monetary losses via the Mean Loss Ratio (MLR), which is defined as the ratio between the repair cost and the insurance value cost (assumed equal to the asset cost). Therefore, the fragility functions are directly converted into mean loss neglecting the uncertainties on the loss for a given damage state. To account for this, we recommend using different cost functions and include these into the logic tree. For example, in Mignan et al. 2015 three cost functions (the Cochrane & Shaad cost function, Cochrane and Shaad, 1992, the RISK-EU cost function, Baisch et al. 2009, and the SERIANEX cost function, Baisch et al. 2009) have been used.

The output of analysis are the so-named loss curves, i.e. probability of exceedance of a given loss normalized to one injection period, for each location of interest. Together with the loss curves, we recommend also to provide loss map distribution for the region of interest based on the probability of exceedance $P(L > l; T) = 10^{-4}$ of the aggregate mean. **Figure 12**a shows the loss map distribution for the region of interest. Figure **12**b shows the mean loss exceedance curves for each building class together with the aggregate loss for a settlement of interest. **Figure 12**c shows the loss exceedance curves for the site of interest together with the epistemic mean, median, 10% and 90% quantiles. The reference project is the Haute-Sorne Enhanced Geothermal System project. Observe that while for hazard the epistemic median was the reference metric for the hazard maps, in financial losses we suggest the epistemic mean value. The same rule we recommend for decision making.

The final operation consists in aggregating losses over the region of interest. Aggregating losses is equivalent to the problem of summing the random variables representing the losses of each settlement. As a practical approach in a preliminary analysis, we recommend to use a stochastic upper bound for the complementary cumulative distribution function (CCDF) of the aggregate loss sum since we know the marginal CCDF of the single local losses but their joint distribution. Despite the dependence structure is unknown, we can assume that the random variables are at most positively dependent. This is corroborated by physical evidence from seismic events. In fact, two closely spaced random variables have generally similar values, while sufficiently distant random variables are expected to have “more” independent values. A stochastic upper bound to the sum of at most positive

dependent random variables is given by considering them perfectly dependents (Dhaene et al., 2012; Broccardo et al., 2017). This correspond to summing quantiles for a given probability level. **Figure 13** reports the loss exceedance curves for the Haute-Sorne Enhanced Geothermal System project.

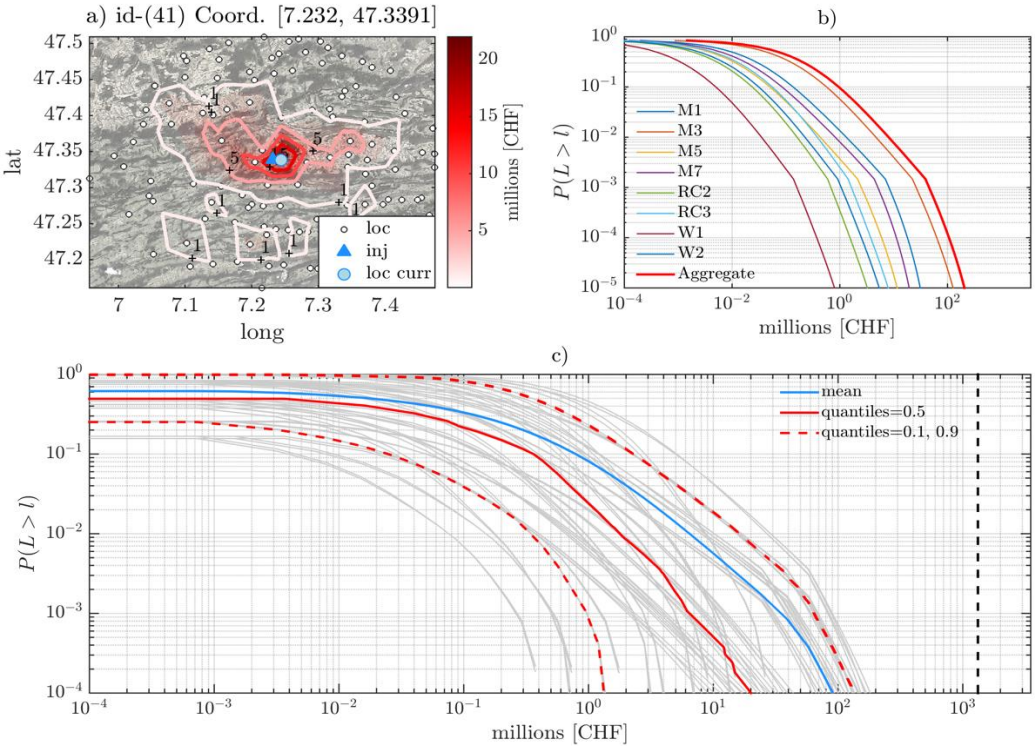

Figure 12: a) Loss map distribution, b) Aggregated losses for different class distributions, and for the site of interest, c) loss exceedance curves for the site id-(41). Black dash line represents the total exposure of the settlement. Broccardo et al. 2019 in preparation.

Finally, we recommend computing the Individual Risk (IR) defined as the annual frequency at which a statistically average individual is expected to experience death or a given level of injury from the realization of a given hazard (Broccardo et al., 2017; Institute of Chemical Engineering, 1992). Following the HAZUS method (Galanis et al., 2018; HAZUS MH MR3, 2003), the IR is computed by convolving the conditional probability of fatality for a given damage level, with the marginal probability of the damage grades. **Figure 14** shows the IR contour for the region of interest based on the maximum epistemic mean of the IR of each class of buildings. **Figure 11**b shows the IR for each class of building for the settlement with highest individual risk (site id-64). Shaded in red, we reported a safety threshold of IR = 10-6, which corresponds to a micromort unit (1 μmt) (Howard, 1980). The individual risk for each settlement is reported in the supplementary material. The results show that the epistemic median and mean of the IR do not cross the 1 μmt threshold at any site of interest. The reference project is the Haute-Sorne Enhanced Geothermal System project.

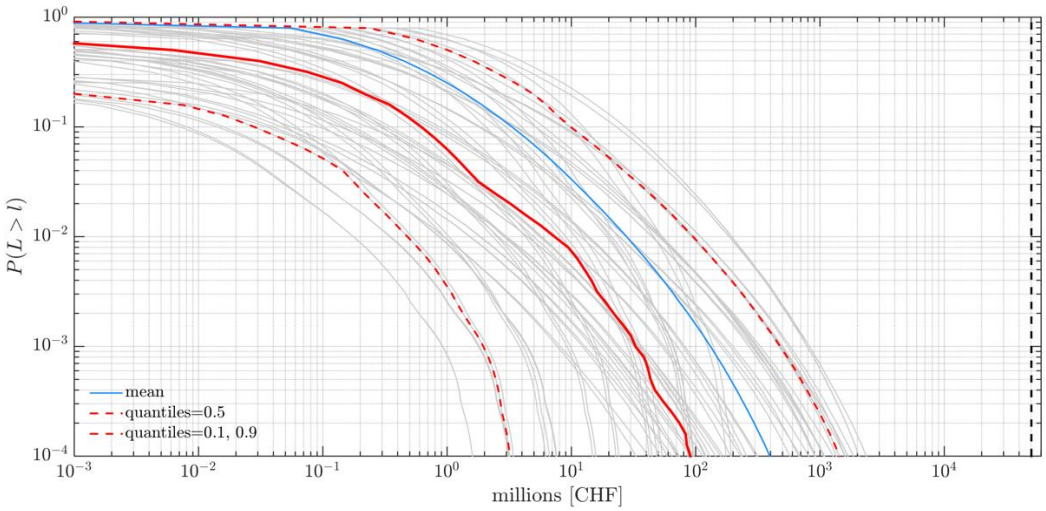

Figure 13: Aggregate losses exceedance curve for the area of interest. The curves represent stochastic upper bounds of the sum of local losses. The black dashed vertical line represents the total building loss. Source: Broccardo et al. 2019 in preparation.

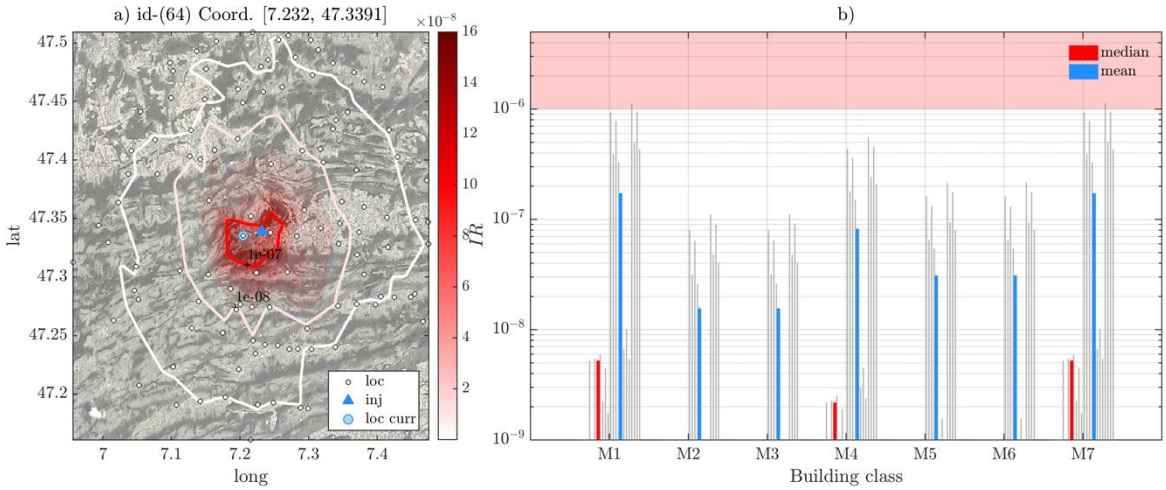

Figure 14: a) Individual risk contours based on the maximum epistemic mean for each class of building. b) Individual risk for a given class building. Red and blue bars are the epistemic median and epistemic mean of the individual risk. Source: Broccardo et al. 2019 in preparation.

Induced seismicity forecast and a-posteriori risk assessment

During the stimulation phase (i.e. reservoir creation phase), earthquakes are a necessary nuisance being a manifestation of "enhancing" the reservoir. Mitigation strategies have been developed to limit induced seismicity, so-called traffic light systems (TLS) (e.g., Bommer et al., 2006; Bosman et al., 2016; Mignan et al., 2017). However, TLS have proven to be less adept to manage post-injection induced seismicity (Majer et al., 2007) and the suitability of TLS for regular reservoir operations has not been widely reported on in the scientific literature. As such, TLSs remain experimental. They are based on a decision variable (such as earthquake magnitude, peak ground velocity, *etc.*) and a threshold above which actions (e.g. stopping or reducing injection/production rates) must be taken. Although the definition of this threshold is currently based on local conditions, expert judgment and regulations (Bosman et al., 2016), Mignan et al. (2017) recently proposed an actuarial approach to induced seismicity risk mitigation where the TLS verifies a specific risk-based safety norm (based on the individual risk *IR*, i.e. the probability that a statistically representative individual dies within a given time window and at a given location). Considering norms and standards already in use in other

hazardous industries (Jonkman et al., 2003), one can now quantify the financial costs of applying a TLS and plan for future EGS plant siting accordingly (Mignan et al., 2019a;b).

The hazard and risk assessment parts of the TLS are not described here, as they are identical to the approach used in the a priori risk assessment (see previous section), with the exception that the parameters a and b now are computed on the fly with a Bayesian procedure explained bellow. Moreover, in addition to the empirical relationship for the injection phase, we introduce a second empirical model for the post-injection phase defined as $\lambda(t;\theta) = 10^{a-bm_0}\dot{V}(t_s)\exp(-\frac{t-t_s}{\tau})$, and t_s is the shut-in time, and τ is the mean relaxation time.

Here, we directly move to the definition of the TLS threshold. With the model of induced seismicity presented in the previous section (which depends on volume injected, *a*, and *b*), one can forecast future seismicity if the injection flow rate is known in advance. A mapping can then be made between modelled seismicity rate and expected damage and risk (following standard methods of probabilistic seismic risk analysis, as shown in the previous section). Finally, for a given quantitative safety norm, say $IR = 10^{-6} = 1$ micromort, one can estimate the magnitude threshold above which injection should be stopped (i.e. TLS) for the norm to be verified (Mignan et al., 2017). This is represented in **Figure 15**. Such a method provides a robust and transparent tool to control induced seismicity based on a specific safety criterion decided by the authorities. This is of course subject to aleatory uncertainty (stochasticity of the process meaning that the norm is only verified on average) and to epistemic uncertainty (the *a*- and *b*-values of the model are not known in advance and may change over time, which requires Bayesian updating; see below). Note that such an approach is safety-norm agnostic. In fact, all safety norms that follow the same iso-risk curve would yield the same TLS.

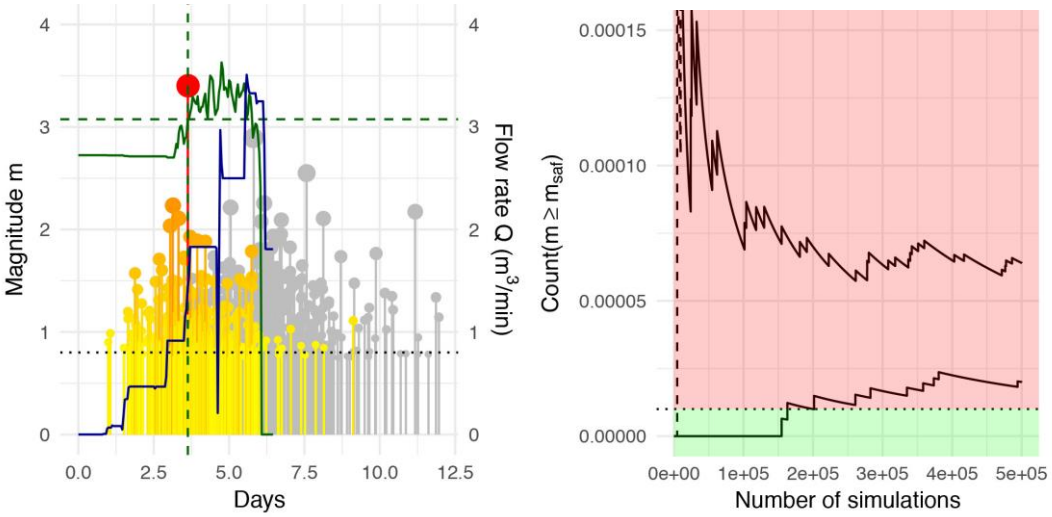

Figure 15: An adaptive TLS in action (in simulations): (left) Induced seismicity time series without ATLS (in grey) compared to a time series where the stimulation is stopped by the ATLS (magnitude threshold represented in green); (right) Verification that the safety standard or norm is respected on average when the ATLS is used (bottom curve) in contrast to no ATLS (top curve) - Rerun from Mignan et al. (2017) as shown in Mignan et al. (2019a).

Real-time updating of fluid-induced seismicity forecasts

In the preliminary hazard analysis, to facilitate standard hazard computations, we suggested to convert the time-variant rate into an equivalent stationary rate. Consequently, the Non-Homogeneous Poisson Process, has been converted into a Homogeneous Poisson Process. However, in the stimulation phase we recommended to use the full Non-Homogeneous Poisson Process and to define an updating scheme to forecast model parameters in real time. In particular, we recommend a hierarchical Bayesian framework (Broccardo et al. 2017) which allows a coherent classification and quantification of the epistemic and aleatory sources of uncertainty.

We prefer a Bayesian approach compared to a frequentist approach, since in the last one, the seismicity rate is assumed to be deterministic. It follows that the uncertainties are only aleatory preventing the possibility of including epistemic uncertainties related to past information resulting from different sites, and to expert judgments and opinions. Moreover, the seismicity-rate models are simply inferred from existing datasets. Although this provides an exact statistical description of the past events, it does not provide a robust online forecasting strategy. Further, the additional knowledge gained cannot be coherently encoded into future project planning.

Alternatively, a hierarchical Bayesian model provides a precise distinction between the sources of uncertainties as well as a consistent online updating strategy. Following the empirical model introduced above, the time-varying rate of the Poissonian process is described as a function of the rate of fluid injection and a set of physical parameters describing underground properties (a, b). First, we suggest to fit with the method of Maximum Likelihood Estimation (MLE) the rate model to existing fluid-induced seismicity sequences; then to use the MLE samples to transform the hyper parameters into random variables to model the uncertainties arising from different sites. A significant advantage of the Bayesian approach is that it enables uncertainties and expert judgments about the model's parameters to be encoded into a joint prior distribution. In this case, we recommend including expert knowledge to determine the bounds of the parameters range. Once the project is started and physical information becomes accessible, the Bayesian framework allows the computation of posterior distribution for the model's parameters, the formulation of predictive models and a robust forecasting strategy. The inference formulation for the empirical model prosed in this paper, together with the predictive model for the number and magnitude of fluid-induced events are reported in detail in Broccardo et al. 2017.

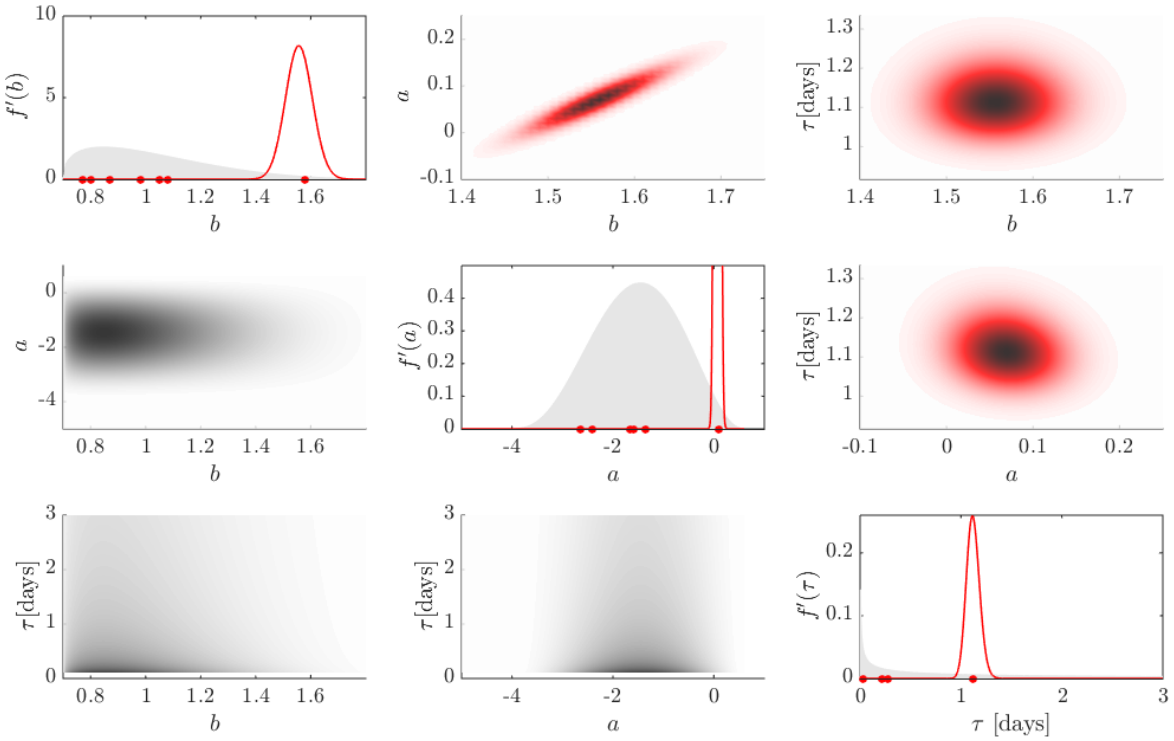

Figure 16: Prior and posterior distribution for Basel 2006 dataset. Diagonal: in shaded grey, the prior distributions, with red lines the posterior distributions, red dots represent MLE estimates from other dates which define the prior distribution. Lower triangular part: joint prior distributions. Upper triangular part: joint posterior distributions. Source: Broccardo et al. 2017

Figure 16 shows the joint prior distribution and the joint posterior after data are available for the Basel 2006 sequence. Observe then even if we have assumed independence in the prior distribution, the posterior distribution encodes the correlation structures emerging from the data, given the observed quantity of interest. In particular, in this case, by observing magnitude and number of events we

observe a positive linear relationship between the parameters a and b. In the figure, it is also reported the parameter τ, which represent mean relaxation time for the post injection phase. As anticipated, even if joint prior distribution is defined based on the independence of model parameters the posterior shows a strong correlation between activation feedback and earthquake size ratio. **Figure 17** shows how the posterior distribution evolution as function of time and data acquisition.

Figure 18 shows the online predictive model for the number of earthquakes and magnitude of events.

Although the proposed rate model reasonably describes the current datasets, different models (e.g. based on geomechanical principles (Gischig and Wiemer, 2013; Catalli et al., 2016; Goertz-Allmann and Wiemer, 2012) or an ensemble of different models (Király-Proag al., 2016) can be used without changing the structure of the proposed framework.

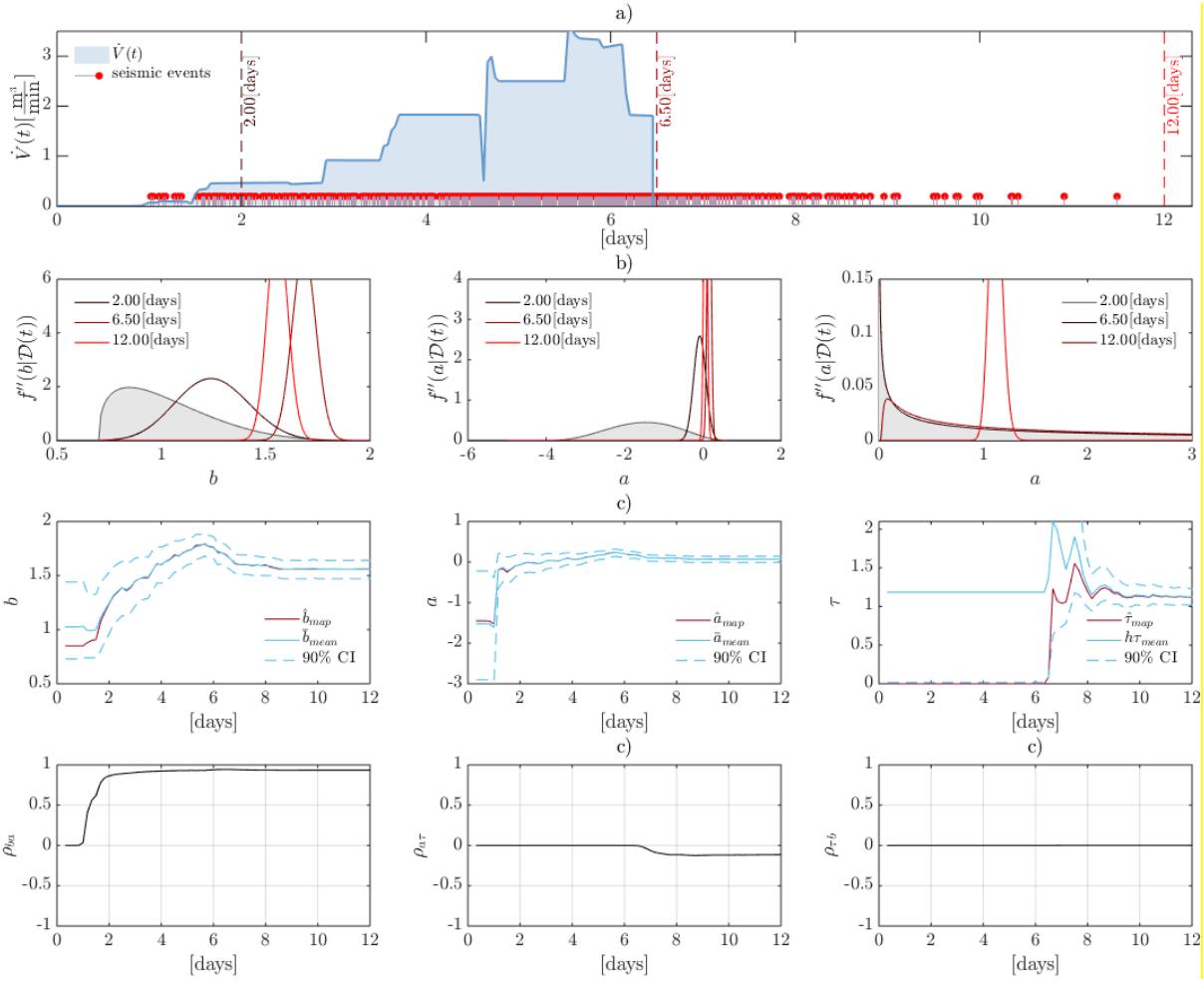

Figure 17: a) Basel 2006 injection profile, and related seismic sequence; b) Marginal model parameter distributions: grey represents prior distributions; c) Evolution over time of the posterior mean and maximum a posterior for each model parameter; d) Time evolution of the correlation coefficient between the model parameters. Source: Broccardo et al. 2017

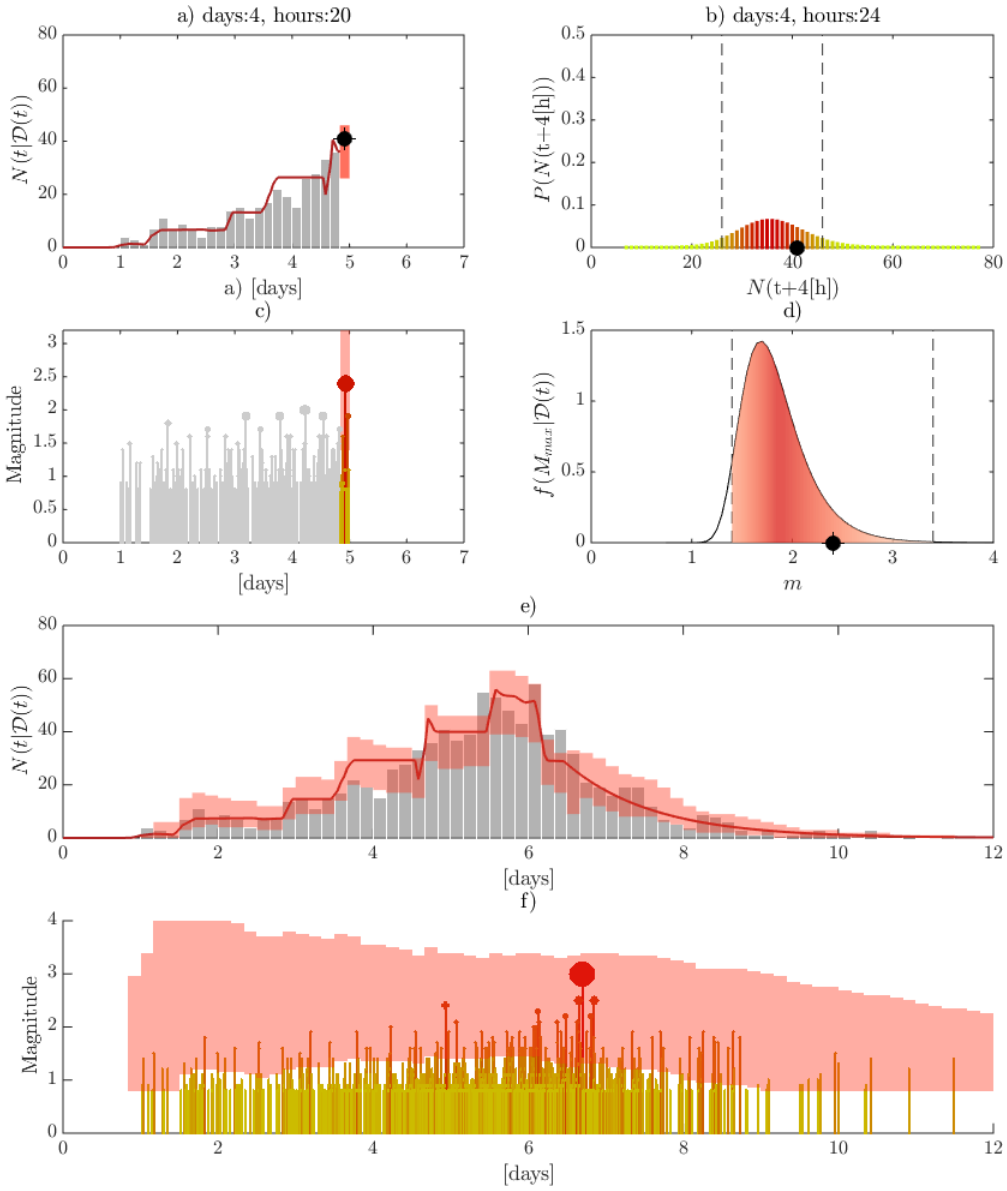

Figure 18: Basel 2006 sequence: a) Prediction of the number of fluid-induced events, red bar Bayesian credible interval, black dot the observed number of events; b) Distribution of the number of seismic events, grey dashed lines credible interval; c) Time series of the magnitude events, red bar asymmetric credible interval for the M_{max}, grey stems past seismic events, yellow-red stems observed seismic event; d) Red area credible asymmetric interval; e) Full prediction of the number of seismic events; d) Full prediction for M_{max}. Source: Broccardo et al. 2017

IV. Conclusions

Finally, it is important to note that decisional protocols should be activity dependent. Indeed, induced seismicity related to hydraulic stimulation of geothermal and hydrocarbon reservoirs generally occur in direct vicinity of the injection well and with no sensible time lag between injection operations and seismicity onset. On the other hand, earthquake triggered by a massive injection of fluids in the subsurface (e.g. wastewater injection operations) may occur at several kilometers distance from the injection wells (Kearenen et al 2013). In a critically stressed crust the pore pressure perturbation generated by such industrial operations may cause the failure of the faults which are favourably oriented with respect to the tectonic stress, identifying these faults prior to fluid injection may help to mitigate the risk associated with induced seismicity. Within this framework modern tools (such as the Adaptive Traffic Light Systems) should be activity-based as well as account for all site-characterization (e.g. ground motion prediction) and preliminary assessment, rather than rely only on magnitudes and or PGA/PGV as in the classical approaches. Finally, the combination of an adequate monitoring infrastructure and advanced processing methods can help to be prepared better and earlier, e.g., promptly allowing a progressive reduction of operations and evaluating the system response before larger earthquakes may take place. The ATLS has been developed within the DESTRESS project test and it is ready to be tested to the DESTRESS demonstration sites of Geldinganes (Iceland) and Bedretto (Switzerland).

V. References

Baisch, S., Koch, C., Stang, H., Pittens, B., Drijver, B., Buik, N. (2016). Defining the framework for seismic hazard assessment in geothermal projects V0.1. ***Technical Report****, Report No. 161005, Bad Bergzabern, Germany: prepared for* Kennis Agenda Aardwarmte.

Bao, X., Eaton, D. W. (2016). Fault activation by hydraulic fracturing in western Canada. ***Science***, aag2583.

Bohnhoff, M., Malin, P., Heege, J. t., Deflandre, J., Sicking, C. (2018). Suggested best practice for seismic monitoring and characterization of non-conventional reservoirs ***First Break***, 36 (2), 59.

Bommer, J. J., Oates, S., Cepeda, J. M., Lindholm, C., Bird, J., Torres, R., Marroquin, G., Rivas, J. (2006). Control of hazard due to seismicity induced by a hot fractured rock geothermal project. ***Engineering Geology****,* 83, 287.

Bosman, K., Baig, A., Viegas, G., & Urbancic, T. (2016). Towards an improved understanding of induced seismicity associated with hydraulic fracturing. ***First Break***, 34(7), 61-66.

Broccardo, M., Mignan, A., Wiemer, S., Stojadinovic, B., Giardini, D. (2017), Hierarchical Bayesian modeling of fluid-induced seismicity. ***Geophysical Research Letters***.

Butcher A., Luckett R., Verdon J. P., Kendall M., Baptie B., Wookey J., (2017), Local Magnitude Discrepancies for Near-Event Receivers: Implications for the U.K. Traffic-Light Scheme, ***Bulletin of the Seismological Society of America***, doi:10.1785/0120160225.

Castagna, J.P., Batzle, M.L, Eastwood, R.L., (1985). Relationships between compressional-wave and shear-wave velocities in clastic silicate rocks. ***Geophysics,*** 50, 571-581.

Catalli, F., Rinaldi, A. P., Gischig, V., Nespoli, M., Wiemer, S. (2016). The importance of earthquake interactions for injection-induced seismicity: Retrospective modeling of the Basel Enhanced Geothermal System. ***Geophysical Research Letters***, 43(10), 4992-4999.

Cesca, S., Grigoli, F. (2015). Chapter Two-Full Waveform Seismological Advances for Microseismic Monitoring. ***Advances in Geophysics,*** 56, 169-228.

Dahm, T. et al. (2013). Recommendation for the discrimination of human-related and natural seismicity. ***Journal of seismology***, 17(1), 197-202.

Daley, T., Freifeld, B.M., Ajo-Franklin, J., Dou, S., Pevzner, R., Shulakova, V., Kashikar, S., Miller, D.E., Goetz, J., Henninges, J., Lueth, S., (2013). Field testing of fiber-optic distributed acoustic sensing (DAS) for subsurface monitoring. ***The Leading Edge***, June 2013, 699-706.

Dahm, T., Cesca, S., Hainzl, S., Braun, T., Krueger, F., (2015). Discrimination between induced, triggered, and natural earthquakes close to hydrocarbon reservoirs: A probabilistic approach based on the modeling of depletion-induced stress changes and seismological source parameters. ***Journal of Geophysical Research: Solid Earth***, 120(4), 2491-2509.

Edwards, B., Douglas, J., (2014). Magnitude scaling of induced earthquakes. ***Geothermics***, 52, 132-139, doi: 10.1016/j.geothermics.2013.09.012.

Ellsworth, W. L. (2013). Injection-Induced Earthquakes. ***Science***, 341 (6142)

Giardini, D. (2009). Geothermal quake risks must be faced. ***Nature***, 462(7275), 848-849.

Gischig, V., S. Wiemer, Alcolea, A. (2014), Balancing reservoir creation and seismic hazard in enhanced geothermal systems, *Geophys J Int*, 198(3), 1585-1598.

Goebel, T. H. W., Hosseini, S. M., Cappa, F., Hauksson, E., Ampuero, J. P., Aminzadeh, F., and Saleeby, J. B. (2016). Wastewater disposal and earthquake swarm activity at the southern end of the Central Valley, California. ***Geophysical Research Letters.***

Goertz-Allmann, B. P., Wiemer, S. (2012). Geomechanical modeling of induced seismicity source parameters and implications for seismic hazard assessment. ***Geophysics***, 78(1), KS25-KS39.

Grigoli, F., Cesca, S., Krieger, L., Kriegerowski, M., Gammaldi, S., Horalek, J., Dahm, T. (2016). Automated microseismic event location using Master-Event Waveform Stacking***. Scientific reports***, 6.

Grigoli, F., Cesca, S., Priolo, E., Rinaldi, A. P., Clinton, J. F., Stabile, T. A., Garcia-Fernandez M., Dost B., Wiemer S., Dahm, T., (2017). Current challenges in monitoring, discrimination, and management of induced seismicity related to underground industrial activities: A European perspective. ***Reviews of Geophysics***.

Grigoli, F., Cesca, S., Rinaldi, A. P., Manconi, A., López-Comino, J. A., Clinton, J. F., Wiemer, S., (2018). The November 2017 Mw 5.5 Pohang earthquake: A possible case of induced seismicity in South Korea. ***Science***, 360(6392), 1003-1006.

Grigoli, F., Scarabello, L., Böse, M., Weber, B., Wiemer, S., & Clinton, J. F. (2018). Pick-and waveform-based techniques for real-time detection of induced seismicity. ***Geophysical Journal International***, 213(2), 868-884.

Hirschberg, S., Wiemer, S., & Burgherr, P. (2015). *Energy from the earth: Deep geothermal as a resource for the future?* Zürich: TA-SWISS Study TA/CD 62/2015, vdf Hochschulverlag AG. doi: https://doi.org/10.3929/ethz-a-010277690

Jousset, P., Reinsch, T., Ryberg, T., Blanck, H., Clarke, A., Aghayev, R., Hersir, G. P., Henninges, J., Weber, M., Krawczyk, C.M., (2018). Dynamic strain determination using fibre-optic cables allows imaging of seismological and structural features, ***Nature Communications*** 9, 2509.

Keranen, K. M., Savage, H. M., Abers, G. A., Cochran, E. S. (2013). Potentially induced earthquakes in Oklahoma, USA: Links between wastewater injection and the 2011 Mw 5.7 earthquake sequence. ***Geology,*** 41(6), 699-702. http://doi.org/10.1130/G34045.1

Kinnaert, X., Gaucher, E., Achauer, U., Kohl, T. (2016). Modelling earthquake location errors at a reservoir scale: a case study in the Upper Rhine Graben. ***Geophysical Journal International***, 206(2), 861-879.

Király-Proag, E., Zechar, J. D., Gischig, V., Wiemer, S., Karvounis, D., Doetsch, J. (2016). Validating induced seismicity forecast models—Induced seismicity test bench. ***Journal of Geophysical Research: Solid Earth***, 121(8), 6009-6029.

Komatitsch, D., Tromp, J., (1999). Introduction to the spectral-element method for 3-D seismic wave propagation. Geophys. J. Int., 139(3), 806-822.

Kraaijpoel, D., Kraft, T., Tramelli, A., De Natale, G., Troise, C., Orazi, M., Jupe, A. (2013). GEISER Deliverable D6.2 - Seismic Monitoring Strategies. INGV, ETHZ, BRGM, NORSAR, KNMI.

Lindsey N. J., Martin, E. R., Dreger, D. S., Freifeld, B., Cole, S., R., James, S. Ajo-Franklin, J. B., (2017). Fiber-optic network observations of earthquake wavefields. ***Geophysical Research Letters***, 44, 11,792–11,799. https://doi.org/10.1002/2017GL075722

Lumens, P.G.E., (2014). Fibre-optic sensing for application in oil and gas wells, ***PhD thesis***, DOI: 10.6100/IR769555

Majer, E., Nelson, J., Robertson-tait, A., Savy, J., & Wong, I. (2012). Protocol for addressing induced seismicity associated with enhanced geothermal systems. Report No. DOE/EE-0662, U.S. ***Department of energy***.

Mateeva, A., Lopez, J., Potters, H., Mestayer, J., Cox, B., Kiyashchenko, D., Wills, P., Grandi, S., Hornman, K., Kuvshinov, B., Berlang, W., Yang, Z., Detomo, R. [2014] Distributed acoustic sensing for reservoir monitoring with vertical seismic profiling. ***Geophysical Prospecting***, 62, 679-692.

McGarr, A., D. Simpson (1997). Keynote lecture: A broad look at induced and triggered seismicity, in ***Rockbursts and Seismicity in Mines***, edited by S. J. Gibowitz and S. Lasocki, pp. 948-970, Balkema, Rotterdam.

Mestayer, J., Grandi Karam, Cox, B., Wills, P., Mateeva, A., Lopez, J, Hill, D., Lewis, A., (2012). Distributed acoustic sensing for geophysical monitoring, Extended abstract for ***EAGE Copenhagen***, Y005.

Mignan, A., Broccardo, M., Wiemer, S., Giardini, D. (2017). Induced seismicity closed-form traffic light system for actuarial decision-making during deep fluid injections. ***Scientific Reports***, 7 (1), 13607.

Mignan, A., Broccardo, M., Wiemer, S., Giardini, D. (2018). Autonomous decision-making against induced seismicity in deep fluid injections. International Symposium on ***Energy Geotechnics***.

Mignan, A., Landtwing, D., Kästli, P., Mena, B., Wiemer, S. (2015). Induced seismicity risk analysis of the 2006 Basel, Switzerland, enhanced geothermal system project: Influence of uncertainties on risk mitigation. ***Geothermics***, 53, 133-146.

Mignan, A., Karvounis, D., Broccardo, M., Wiemer, S., Giardini, D. (2019). Including seismic risk mitigation measures into the Levelized Cost Of Electricity in enhanced geothermal systems for optimal siting. ***Applied Energy***, 238, 831-850.

Ogwari, P. O., Horton, S. P., Ausbrooks, S. (2016). Characteristics of Induced/Triggered Earthquakes during the Startup Phase of the Guy-Greenbrier Earthquake Sequence in North-Central Arkansas. ***Seismological Research Letters***.

Schaff, D. P., Waldhauser, F. (2005). Waveform cross-correlation-based differential travel-time measurements at the Northern California Seismic Network. ***Bulletin of the Seismological Society of America***, 95(6), 2446-2461.

Shapiro, S., O. S. Kruger, Dinske, C. (2013). Probability of inducing given-magnitude earthquakes by perturbing finite volumes of rocks, ***J. Geophys. Res. Solid Earth***, 118, 3557-3575, doi:10.1002/jgrb.50264.

Skoumal, R. J., Brudzinski, M. R., Currie, B. S. (2015). Distinguishing induced seismicity from natural seismicity in Ohio: Demonstrating the utility of waveform template matching. ***Journal of Geophysical Research: Solid Earth***, 120(9), 6284-6296.

Tromp, J., Komatitsch, D., Liu, Q., (2008), Spectral-element and adjoint methods in seismology. Commun. ***Comput.Phys***., 3(1), 1–32.

Trutnevyte, E., Wiemer, S. (2017). Tailor-made risk governance for induced seismicity of geothermal energy projects: An application to Switzerland. ***Geothermics***, 65, 295-312.

Yoon, C. E., O'Reilly, O., Bergen, K. J., Beroza, G. C. (2015). Earthquake detection through computationally efficient similarity search. ***Science advances***, 1(11), e1501057.

Waldhauser, F., Ellsworth, W. L. (2000). A double-difference earthquake location algorithm: Method and application to the northern Hayward fault, California***. Bulletin of the Seismological Society of America***, 90(6), 1353-1368.

Waldhauser, F., Schaff, D. P. (2008). Large-scale relocation of two decades of northern California seismicity using cross-correlation and double-difference methods. **Journal of Geophysical Research: Solid Earth**, 113(B8).

Waldhauser, F. (2009). Near-real-time double-difference event location using long-term seismic archives, with application to Northern California, ***Bull. Seism. Soc. Am***., 99, 2736-2848, doi:10.1785/0120080294.

Imprint

Project Lead
GFZ German Research Centre for Geosciences
Telegrafenberg
14473 Potsdam (Germany)
www.gfz-potsdam.de/en/home/

Project Coordinator
Prof. Ernst Huenges
huenges@gfz-potsdam.de
+49 (0)331/288-1440

Project Manager
Dr. Justyna Ellis
ellis@gfz-potsdam.de
+49 (0)331/288-1526

Project Website
www.destress-h2020.ch

Report Authorship
Grigoli F., Broccardo M., Mignan A., Paap B., Verdel A., Wiemer S. (2019). Workflows for seismic risk assessment for soft stimulations, ***Destress report***, Deliverable D3.2, February 2019, 32 pp.

Liability claim

DESTRESS is co-funded by

National Research Foundation of Korea (NRF)
Korea Institute for Advancement of Technology (KIAT)
Swiss State Secretariat for Education, Research and Innovation (SERI)